Ultramicroscopy 111 (2011) 1461–1468

Contents lists available at ScienceDirect

Ultramicroscopy

journal homepage: www.elsevier.com/locate/ultramic

Theory of free electron vortices

P. Schattschneider [a,b,*], J. Verbeeck [c]

[a] Institute for Solid State Physics, Vienna University of Technology, A-1040 Wien, Austria
[b] Service Centre for Electron Microscopy, Vienna University of Technology, A-1040 Wien, Austria
[c] EMAT, University of Antwerp, B-2020 Antwerp, Belgium

ARTICLE INFO

Article history:
Received 16 February 2011
Received in revised form
4 July 2011
Accepted 14 July 2011
Available online 23 July 2011

Keywords:
TEM
Coherence
Angular momentum
Vortex beams

ABSTRACT

The recent creation of electron vortex beams and their first practical application motivates a better understanding of their properties. Here, we develop the theory of free electron vortices with quantized angular momentum, based on solutions of the Schrödinger equation for cylindrical boundary conditions. The principle of transformation of a plane wave into vortices with quantized angular momentum, their paraxial propagation through round magnetic lenses, and the effect of partial coherence are discussed.

1. Introduction

Electron vortices are free electrons carrying orbital angular momentum. They are characterized by a spiraling wavefront with a screw dislocation along the propagation axis. With the publication of two seminal papers on the creation of electron vortices in the electron microscope [1,2] the matter was transformed from a theoretical possibility [3] to reality. The first practical application was a filter for magnetic transitions in the ferromagnetic 3d metals, thus facilitating experiments in the field of energy loss magnetic chiral dichroism (EMCD) [4]. The potential of vortices is much wider, ranging from probing chiral structures to manipulation of nanoparticles, clusters and molecules, exploiting the magnetic interaction [5].

For a review of vortex applications in optics, see [6]. The theory of field vortices was first described in the 1970s [7] in the context of dislocations in sound waves; it took almost one decade before such vortices in the optical frequency range were produced [8]. It was then realized that optical vortices were related to angular momentum of light, which already Poynting in 1909 speculated about [9]. The two formerly rather separated fields of research began to merge. The first experimental demonstration of laser light carrying *quantized* orbital angular momentum came in 1992 [10].

In the context of orbital angular momentum optical vortices are similar to electron vortices. In a sense, the latter are simpler than optical ones because the electron is described by a scalar wave equation[1] (the Schrödinger equation) whereas optical vortices are vector fields. But for unpolarized light the description of vortex modes can be simplified, and in the paraxial approximation they have in fact been described by a Schrödinger type equation [11]. One of the surprising and original features of electron vortices is that, according to their rotational component of probability current they carry also a magnetic moment, even for beams without spin polarization. This, together with the much smaller scale of electron vortices compared to light, makes them so attractive.

We present here a theory of electron vortices based on solutions of the Schrödinger equation. We assume cylindrical geometry, starting with the general case allowing external scalar and vector potentials. Then we concentrate on potential-free systems, having in mind vortices propagating freely in space.[2] It turns out that the solutions fall into families with quantized angular momentum $\hbar m$ along the optic axis.

2. The Schrödinger equation in cylindrical geometry

We assume an electron propagating along the z axis of the microscope and defined within a circle of radius r_M (the aperture). There may or may not be a magnetic field present in the space where the free electron propagates. We look for the general

* Corresponding author at: Institute for Solid State Physics, Vienna University of Technology, A-1040 Wien, Austria.
E-mail address: schattschneider@ifp.tuwien.ac.at (P. Schattschneider).

0304-3991/$ - see front matter © 2011 Elsevier B.V. All rights reserved.
doi:10.1016/j.ultramic.2011.07.004

[1] For standard electron microscope probes, which are not spin polarized.
[2] The magnetic field of the lenses in the electron microscope is weak enough such that its effect can be compensated by assuming a slowly rotating reference frame during propagation through the lens [12].

solution of the Schrödinger equation. A natural coordinate system is cylindrical for this geometry. The Hamilton operator in SI units is

$$H=\frac{1}{2M}(\hat{p}-e\hat{A})^2+e\hat{V}, \tag{1}$$

where M is the electron mass, e its charge, $\hat{A}$ and $\hat{V}$ are the vector and scalar potential operators, and $\hat{p}$ is the momentum operator. The first term can be written as

$$\hat{p}^2-e(\hat{p}\hat{A}+\hat{A}\hat{p})+e^2\hat{A}^2.$$

With $\nabla(\hat{A}\psi)=\psi\nabla\hat{A}+\hat{A}\nabla\psi$ and (in Coulomb gauge) $\nabla\cdot\hat{A}=0$, so that

$$H=\frac{1}{2M}(\hat{p}^2-2eA\hat{p}+e^2\hat{A}^2)+e\hat{V}. \tag{2}$$

We write the time-independent Schrödinger equation

$$H|\psi\rangle=E|\psi\rangle$$

in cylindrical coordinates (r,φ,z). In these coordinates the nabla operator reads

$$\nabla=\left(\frac{\partial}{\partial r},\frac{\partial}{r\partial\varphi},\frac{\partial}{\partial z}\right).$$

Now that $\hat{p}=-i\hbar\nabla$ we have

$$\hat{A}\hat{p}=-i\hbar\left(A_r\frac{\partial}{\partial r}+\frac{A_\phi}{r}\frac{\partial}{\partial\varphi}+A_z\frac{\partial}{\partial z}\right),$$

$$\hat{p}^2=-\hbar^2\left(\frac{\partial^2}{\partial r^2}+\frac{\partial}{\partial r}+\frac{\partial^2}{r^2\partial\varphi^2}+\frac{\partial^2}{\partial z^2}\right).$$

For the special case of a constant magnetic field along z and a vanishing electrostatic potential $V=0$ (which will be important as an approximation to magnetic lenses in a follow-up paper) we can conveniently use a gauge where $A_r=A_z=0$, so

$$A^2=A_\phi^2.$$

The Schrödinger equation with Hamiltonian Eq. (1) reads

$$\frac{-\hbar^2}{2M}\left[\frac{\partial^2}{\partial r^2}+\frac{\partial}{r\partial r}+\frac{\partial^2}{r^2\partial\varphi^2}+\frac{\partial^2}{\partial z^2}-i\frac{2eA_\phi}{\hbar r}\frac{\partial}{\partial\varphi}-\left(\frac{eA_\phi}{\hbar}\right)^2\right]\psi=E\psi. \tag{3}$$

Separation of variables

$$\psi(r,\varphi,z)=R(r)Y(\varphi)Z(z) \tag{4}$$

inserted into Eq. (3) transforms the partial derivatives into simple derivatives

$$\frac{R''}{R}+\frac{R'}{rR}-i\frac{2eA_\phi}{\hbar}\frac{Y'}{rY}+\frac{Y''}{r^2Y}+\frac{Z''}{Z}-\left(\frac{eA_\phi}{\hbar}\right)^2=-\frac{2ME}{\hbar^2}. \tag{5}$$

The separation of variables is consistent with the fact that the Hamiltonian of a rotationally invariant system (free space or a radially symmetric vector potential) commutes with $\hat{L}_z$ and with $\hat{P}_z$; as a consequence, the eigenfunctions of $\hat{P}_z$:

$$Z\propto e^{izk_z} \tag{6}$$

and of $\hat{L}_z$:

$$Y\propto e^{im\varphi}, \tag{7}$$

where m is integer because it must be 2π-periodic in the azimuth due to periodic boundary conditions are also eigen functions of the Hamiltonian.

3. Electrons in field free space

We consider the case of an electron limited by a circular aperture. We also assume that no potentials exist. The case of non-vanishing magnetic flux will be considered elsewhere.

3.1. Boundary conditions

The boundary condition at the rim of an aperture of radius r_M centered at the origin is

$$R(r_M)=0. \tag{8}$$

We look for solutions inside the aperture consistent with Eq. (8) and match them with the trivial solution outside the aperture $R(r\geq r_M)=0$. Since we deal with free electrons there are no scalar or vector potentials. Expressing the energy E of the electron by the wave number of its plane wave solution

$$E=\frac{\hbar^2k_0^2}{2M}, \tag{9}$$

multiplying Eq. (5) with r^2, filling in solutions Eqs. (6) and (7), and rearranging terms we obtain the differential equation

$$r^2\frac{R''}{R}+r\frac{R'}{R}+r^2k_r^2-m^2=0 \tag{10}$$

for the radial part of the wave function. We have used the abbreviation

$$k_r=\sqrt{k_0^2-k_z^2}. \tag{11}$$

The substitution $x=rk_r$ and $y(x):=R(x/k_r)$ yields

$$x^2\frac{y''}{y}+x\frac{y'}{y}+x^2-m^2=0. \tag{12}$$

This is Bessel's differential equation. The solutions are Bessel functions of the first kind J_m and the second kind Y_m with index m. The Y_m are divergent at $x=0$ and can be excluded for round apertures centered on the optic axis. The radial solutions

$$J_m(x)=J_m(rk_r) \tag{13}$$

are indexed according to quantum numbers k_r and m. The factor $Z(z)$ depends on the quantum number k_z. The energy spectrum is given by Eq. (9) as

$$E_{k_r,k_z}=\frac{\hbar^2}{2M}(k_r^2+k_z^2)>0.$$

Note that the energy is always positive because the particle is free. States are degenerate in the magnetic quantum number m. Note that without magnetic field m is integer.[3] It is important to note that the parameter k_r is real since $k_z\leq k_0$.

3.2. Special case

The special case $k_r=0$ gives a particular solution

$$R(r)\propto r^{\pm m}.$$

In order to avoid singularities at $r=0$ the exponent must be positive; it must also vanish at the rim of the beam defining aperture with radius $r=r_M$ which is impossible for $m\neq 0$. For $m=0$ the solutions read (going back to Eq. (12) for this special case)

$$R\propto(r^2-r_M^2).$$

That is to say that $k_r=0$ does not allow solutions with $m\neq 0$, nor a constant intensity within the aperture That means that $m\neq 0$

[3] Non-zero magnetic fields define a complete set of Bessel functions with non-integer index.

solutions inevitably have $\langle k_r \rangle > 0$ and $\langle k_z \rangle < k_0$. In the next section we discuss properties of beams with discrete angular momentum, including $\langle \hat{L}_z \rangle = 0$.

3.3. Solutions with quantized angular momentum

The general solution of the present problem for $k_r > 0$, Eq. (4), is

$$\psi(r,\varphi,z) = e^{izk_z} e^{im\varphi} J_m(rk_r).$$

It is convenient to classify the solutions according to the eigenvalue m of Eq. (7), as

$$\psi_m(r,\varphi,z) = e^{izk_z} e^{im\varphi} \sum_{k_r} c(k_r) J_m(rk_r), \tag{14}$$

with arbitrary coefficients $c(k_r)$. The reason is that ψ_m is an eigenfunction of $\hat{L}_z$ with eigenvalue $\hbar m$. To see this, one may calculate the expectation value directly: the angular momentum of the electron is

$$\langle \hat{L}_z \rangle = \langle \psi | \hat{L}_z | \psi \rangle.$$

In cylindrical coordinates the angular momentum operator reads

$$\hat{L}_z = -i\hbar \frac{\partial}{\partial \varphi}.$$

For solutions belonging to the J_m family, Eq. (14) we find

$$\langle \hat{L}_z \rangle = -i\hbar \int \psi^* \frac{\partial}{\partial \varphi} \psi \, dV = \hbar m \int \rho \, dV = \hbar m. \tag{15}$$

The boundary condition Eq. (8) reduces the allowed values of k_r to a discrete set

$$k_r \in \{\lambda_{nm}/r_M, n \in \mathbb{N}\},$$

where the λ_{nm} are the zeros of the Bessel function J_m. For $m=0$ a frequent situation is given by a wave function that is constant within the round aperture and vanishes outside, $\psi_0 = \Pi(r/r_M)$ where Π is the radial step function

$$\Pi(x) = \begin{cases} 1, & x \le 1, \\ 0, & x > 1. \end{cases}$$

Expanding ψ_0 into eigenfunctions of this geometry we obtain

$$\Pi(r/r_M) = \sum c_n J_0(\lambda_n r/r_M), \tag{16}$$

with

$$c_{n0} = \frac{2}{\lambda_n J_1(\lambda_{n0})},$$

which by definition of the zeros λ_{n0} vanishes at the rim $r = r_M$. This gives a set of

$$\left\{ k_{z,n} = \sqrt{k_0^2 - (\lambda_{n0}/r_M)^2}, n \in \mathbb{N} \right\}.$$

As a demonstration example we assume an aperture of 1 μm in Fig. 1; the first 10 coefficients give already a good approximation. This solution is of type J_0; from Eq. (7), its angular momentum is $\langle \hat{L}_z \rangle = 0$.

The relative deviations of k_z from k_0 for a 200 kV incident beam are of the order of 10^{-10} which translates into 10^{-5} eV, so the splitting of the k_z levels is unobservable in practice. The set of different k_r creates the oscillations within the aperture, visible in Fig. 1. In combination with the set of k_z they propagate the solution into z direction.

For $m=1$, the solutions are Bessel functions J_1. By analogy to the case $m=0$ we find the expansion for a wave with constant *amplitude* in the aperture in the family J_m, $\psi_m = e^{ik_z z} e^{im\varphi} \Pi(r/r_M)$:

$$\psi_m(r,\varphi,z) = e^{ik_z z} e^{im\varphi} \sum c_{nm} J_1(\lambda_n r/r_M).$$

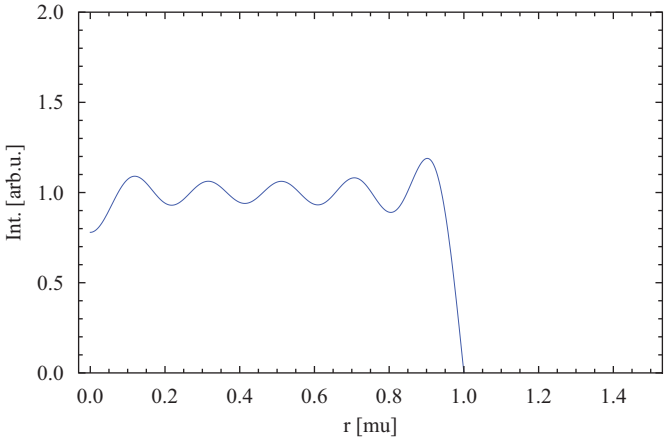

Fig. 1. Plane wave filling a round aperture of 1 μrad. First 10 basis functions.

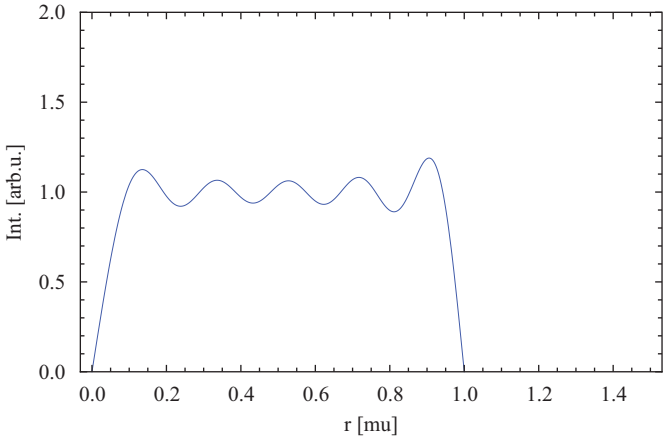

Fig. 2. Amplitude of a helical wave with $m=1$ filling a round aperture of 1 μrad. First 10 basis functions.

The result is given in Fig. 2. Contrary to the $m=0$ case, we see here the amplitude dropping to zero at the origin despite the fact that we assumed a constant amplitude. Expansion to higher order will make the slope steeper, eventually leaving a 'pinhole' at the origin. This is a consequence of the central vortex line where the phase is undefined, also known as topological charge.

4. Focussed vortices

The solutions discussed in the previous section had constant amplitude over the aperture. Can we focus such extended beams? The case $m=0$ is trivial—it is exactly what happens when one illuminates an aperture in the electron microscope with a plane wave. An ideal lens will create an Airy disk in the diffraction (back focal) plane. The action of the lens is described by a Fourier transform.

We can perform such transforms for beams with any quantum number $m \neq 0$. According to the Fourier–Bessel transform of a function $F = f(r)e^{im\varphi}$ with azimuth angle φ,

$$\tilde{F}(\mathbf{q}) = \frac{i^m}{2\pi} e^{im\varphi} \int_0^{r_M} f(r) J_m(qr) r \, dr,$$

the Fourier transform of ψ_m is

$$\tilde{\psi}_m(\mathbf{q}) = \frac{i^m}{2\pi} e^{im\varphi} \int_0^{r_M} J_m(qr) r \, dr. \tag{17}$$

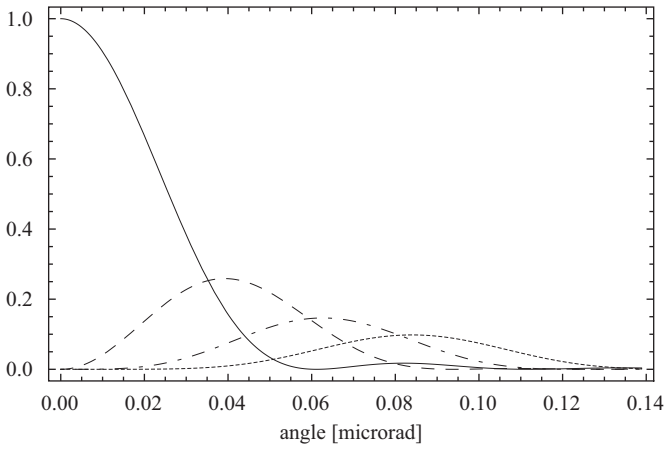

Fig. 3. Radial intensity distribution scaled to the maximum value in the back focal (i.e. diffraction) plane of a lens for vortex waves filling a round aperture of 50 μm diameter, with $m=0$ (full line) $m=1$ (dashed), $m=2$ (dash-dotted), and $m=3$ (dotted). $C_s=0$, 200 kV. Abscissa: scattering angle in μrad. Zero denotes the vortex centers.

We may calculate the far field solution via Eq. (17), equivalent to the diffraction pattern produced by an ideal lens. The intensity $I_m(q)=|\psi_m|^2$ is isotropic. The radial intensity profiles are shown in Fig. 3. Only the $m=0$ beam has a maximum at the center; it is the well known Airy disk. The vortex beams are characterized by a ringlike structure with a maximum position depending on the helicity m. Note that contrary to intuition, according to Plancheret's theorem, the total intensity is equal for each m provided the ψ_m are equally normalized. The helicity of a beam can then be determined by measuring the intensity as a function of momentum $q=|\mathbf{q}|$. This is the basis for further analysis of vortex beams. It should be noted that the focussed vortex has the same angular momentum as the original one since the azimuthal part is still of type $e^{im\varphi}$. More generally, after passage through the mask, the electron remains in the same eigenstate of the angular momentum operator because the angular momentum is a constant of motion in free space.

4.1. Arbitrary wave forms

Any wave function can be expanded into the eigenfunctions of the cylindrical geometry described here,

$$\psi(\mathbf{r})=\sum_m f_m(r)e^{im\varphi}.$$

Its FT is

$$\tilde{\psi}(\mathbf{q})=\sum_m \frac{i^m}{2\pi}e^{im\varphi}\int_0^\infty f_m(r)J_m(qr)r\,dr=\sum_m \frac{i^m}{2\pi}e^{im\varphi}\tilde{f}_m(q). \tag{18}$$

For amplitudes $f_m(r)$ defined within a finite aperture one may use a series expansion similar to Eq. (16).

$$f_m(r)=\sum_n c_{nm}J_m(\lambda_{n,m}r/r_M),$$

with

$$c_{nm}=\frac{2}{r_M^2J_{m+1}^2(\lambda_{n,m})}\int_0^{r_M} f_m(r)J_m(\lambda_{n,m}r/r_M)r\,dr.$$

Evaluating the transform Eq. (17) at positions $q=\lambda_{n,m}/r_M$, one can apply the orthogonality relations for Bessel functions. The result is

$$\tilde{f}_m(\lambda_{n,m}/r_M)=\frac{r_M^2i^m}{4\pi}\sum_n c_{nm}J_{m+1}^2(\lambda_{n,m}) \tag{19}$$

as can be verified by inserting the c_n. Eventually,

$$\tilde{\psi}(\mathbf{q})=\frac{r_M^2}{8\pi^2}\sum_{mn} i^{2m}e^{im\varphi}c_{nm}J_{m+1}^2(\lambda_{n,m}). \tag{20}$$

Note that each m has different zeroes $\lambda_{n,m}$.

5. Creation of vortex electrons

Vortex electrons can be created with spiral phase plates [1] or with holographic masks [2]. We illustrate the working principle underlying the creation of electron vortices, a plane wave passing through a holographic mask. Since the subject of this paper is the theory of electron vortices and not any technical aspect we restrict the discussion to the elementary form of a fork dislocation in the following.[4]

A plane wave is by definition infinitely extended and can therefore not be a solution of the present case. We ask for solutions that match a plane wave within the aperture and vanish outside. I.e. we simulate a plane wave e^{ik_zz} impinging onto a round aperture with absorptive structure given by the transmission function

$$T=\tfrac{1}{2}\Pi(r/r_M)(1-\cos(\mathbf{k}_x\mathbf{r}-\varphi)), \tag{21}$$

where φ is the azimuthal angle in the aperture plane, and $k_x=2\pi/d$ with the lattice distance d. The exit wave function is

$$\psi=e^{ik_zz}T=e^{ik_zz}(\tfrac{1}{2}\Pi(r/r_M)+e^{-i\mathbf{k}_x\mathbf{r}}\Pi(r/r_M)e^{\varphi}+e^{i\mathbf{k}_x\mathbf{r}}\Pi(r/r_M)e^{-\varphi}), \tag{22}$$

where k_z is the wave number of the fast electron that propagates in the z direction. Matching this wave function to the boundary conditions of cylindrical geometry means a decomposition of ψ into eigenfunctions of a round aperture. We have already encountered the first term in brackets—expression 16 for a plane wave. The other terms belong to the family of vortex solutions with $m=\pm1$,

$$\psi_m(\mathbf{r})\propto\Pi(r/r_M)e^{im\varphi}. \tag{23}$$

The phase factor $e^{\pm ik_xx+k_zz}$ describes propagation of the partial waves under the angle $\pm\arctan(k_x/k_z)$ with respect to the optic axis, in direction $\mathbf{k}_x$, caused by diffraction on the periodic mask.[5] The transmission function of the holographic mask is shown in Fig. 4.

The diffraction pattern of the holographic mask is shown in Fig. 5. The phase of the wave function is coded as hue, the range $[-\pi,\pi]$ corresponding to colours continuously changing from blue to red (rainbow chart). The central Airy disk and its first two concentric rings are well visible. The $m=\pm1$ side bands show the characteristic volcano shape of vortices.[6] Whereas the central Airy disk has a cylinder symmetric phase, the vortices show azimuthal phase variation over 2π. Compare also the radial phase jumps at the central pattern (blue to red to blue) with the more gradual phase variations at the vortices. A trace through the diffraction pattern is shown in Fig. 6. Here the typical volcano profile of the side bands is clearly visible.

[4] At the time of writing spiral phase plates have been demonstrated, but are less reliable. Also real fork holographic masks are different from the chosen demonstration example inasmuch as they create higher order side bands.

[5] One can compensate this sideways deviation for one of the side bands by imposing an initial phase $\mp k_xx$ onto the incident plane wave.

[6] Real marks have sharp edges. These edges give rise to higher harmonics in the Fourier transform, and those harmonics will create vortices with higher quantum number m. We will not deal with this case here.

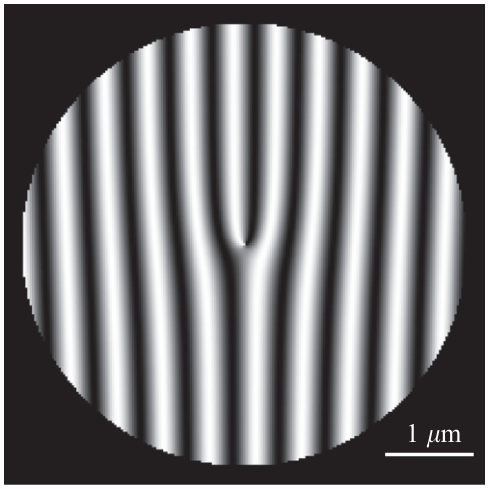

Fig. 4. Transmission function Eq. (21) for creating vortex beams. The aperture has 5 μm diametre. Scale in μm.

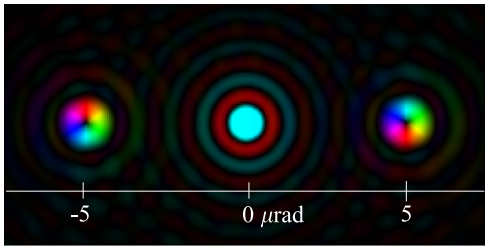

Fig. 5. Diffraction pattern of the mask in Fig. 4 obtained by Fourier transform, showing the central Airy disk and two focussed vortices. The Bragg angle at 200 kV is 2.5 μrad. The phase is coded as hue. The helical structure of the vortices is well visible (Color coding: Rainbow chart from 0 to 2π). (For interpretation of the references to color in this figure legend, the reader is referred to the web version of this article.)

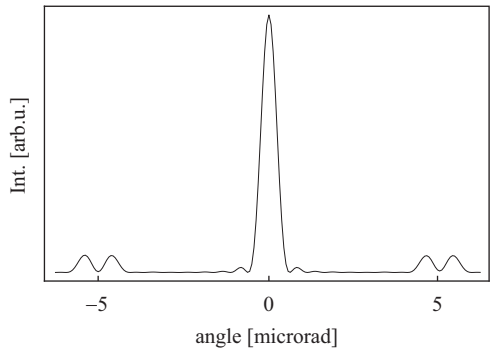

Fig. 6. Horizontal trace through the diffraction pattern shows the volcano-like profiles of the vortices. Scale in μrad.

6. Spherical aberration

The focussed vortices of Fig. 5 with wave functions $\tilde{\psi}$ given by Eq. (17) are in the far field, or – equivalently – in the diffraction (back focal) plane of an ideal lens. Spherical aberration and defocus distort this ideal wave function via the wave transfer function W describing the wave front aberrations of the lens as

$$\tilde{\phi}(\mathbf{q}) = \tilde{\psi}(\mathbf{q}) \otimes W(\mathbf{q}).$$

This can be written as a product of the Fourier transformed functions

$$\phi(\mathbf{\Theta}) = \psi(\mathbf{\Theta})\tilde{W}(\mathbf{\Theta}),$$

with the wave front aberration χ and the aperture defining function Π:

$$\tilde{W}(\mathbf{\Theta}) = \Pi(\Theta/\Theta_M)e^{i\chi(\mathbf{\Theta})}.$$

Note that $\mathbf{\Theta}$ is the variable after Fourier transform from the $\mathbf{q}$ plane. The beam defining aperture appears under a half angle Θ_M (i.e. the half convergence angle seen from a point in the $\mathbf{q}$ plane). Taking into account only defocus df and spherical aberration C_s the phase imposed by the lens is radially symmetric, e.g. [13],

$$\chi(\Theta) = \frac{k_z}{2}\left(df\Theta^2 + \frac{C_s}{2}\Theta^4\right).$$

Note that the scattering angle $\mathbf{\Theta}$ relates to the coordinate $\mathbf{r}$ in the aperture as $\mathbf{\Theta} = \mathbf{r}/f$ for a lens of focal length f (provided that $\Theta \ll 1$). Eq. (17) for the perfect lens is now replaced by

$$\tilde{\psi}_m(\mathbf{q}) = \frac{i^m}{2\pi}e^{im\varphi}\int_0^{r_M} e^{i\chi(r/f)}J_m(qr)r\,dr, \tag{24}$$

which we evaluate at the Scherzer defocus $df = -\sqrt{C_s\lambda}$. The azimuth angle φ is now in the diffraction plane where the vortex is focussed. In Figs. 7–9 are shown the radial traces through the intensity patterns for different aperture/mask diameters. For an ideal lens the profiles would be identical with the profile over the right or left vortex in Fig. 5. The angle is measured with respect to the center of the vortex (which is at 5 μrad in Fig. 5).

The maxima of the $m > 0$ vortices move to higher radii with increasing aberration. For the largest mask the change is well visible; less for the 50 μm mask, and negligible for the small mask. The side maxima in the profiles increase with m and with the aberration constant. Interestingly, the central zero for the vortices with $|m| > 0$ remains always zero independent of the aberration. The vortex diameter scales with the reciprocal aperture size. Even for the smallest mask it is in the range of μrad. Such structures are difficult to observe.[7]

7. Incoherent illumination

In reality, a perfectly coherent probe does not exist. Rather we have illumination with extended sources, which reduces the spatial (lateral) coherence of the beam. The grade of coherence is given by the angle subtended by the source on the aperture, i.e. the convergence angle. An exact treatment of partial coherence would involve calculation of the density matrix of the electron. Although only diagonal terms of this matrix are observable, the off-diagonal terms which are closely related to the mixed dynamic form factor [14,15] may lead to visible effects when the electron interacts with matter [16–18]. The incoherent superposition of waves coming from different points in the source reduces the size of the coherence patch on the aperture. This gives rise to a broadening of the diffraction spots. The resulting vortex profiles are calculated from a convolution of Eq. (17) with the incoherent intensity distribution of the source, projected on the diffraction plane. We assume here a Gaussian source shape

$$\rho_s = e^{-\mathbf{q}^2/2\sigma^2}.$$

With the charge density in the back focal plane from a perfectly coherent (point) source

$$\rho = |\tilde{\psi}_m(\mathbf{q})|^2,$$

[7] Extremely large camera lengths are necessary. This can be achieved in the low-angle diffraction mode.

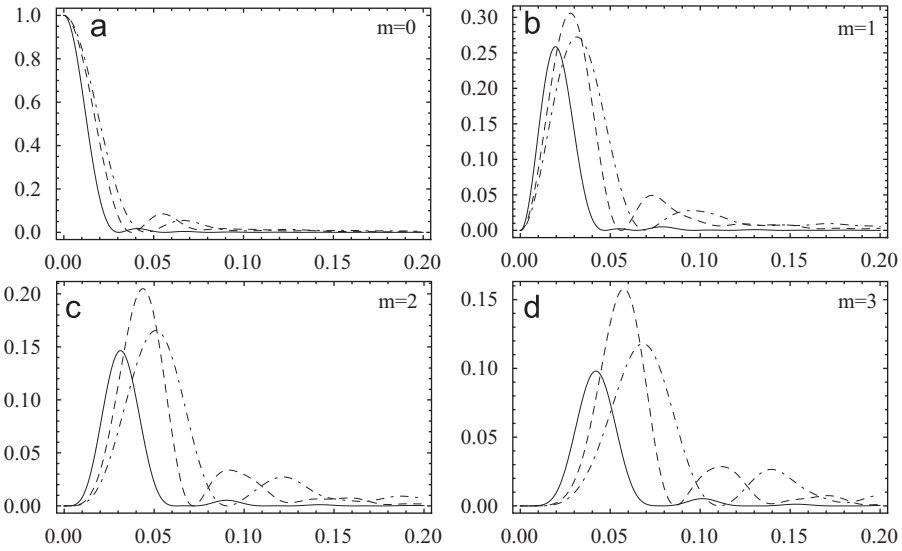

Fig. 7. Radial intensity profiles in the diffraction plane at Scherzer defocus for different spherical aberration constants, 200 kV. Mask with 100 μm diameter. Abscissa: scattering angle in μrad. Zero denotes the vortex centers, as in Fig. 3. Full lines for $C_s=0$, dashed lines $C_s=0.5$ mm, dash-dotted lines $C_s=1.2$ mm. The panels a–d are for quantum numbers $m=0$, 1, 2, 3. The abscissa is relative to the vortex centres in μrad. The profiles are scaled to the maximum of the $m=0$ beam.

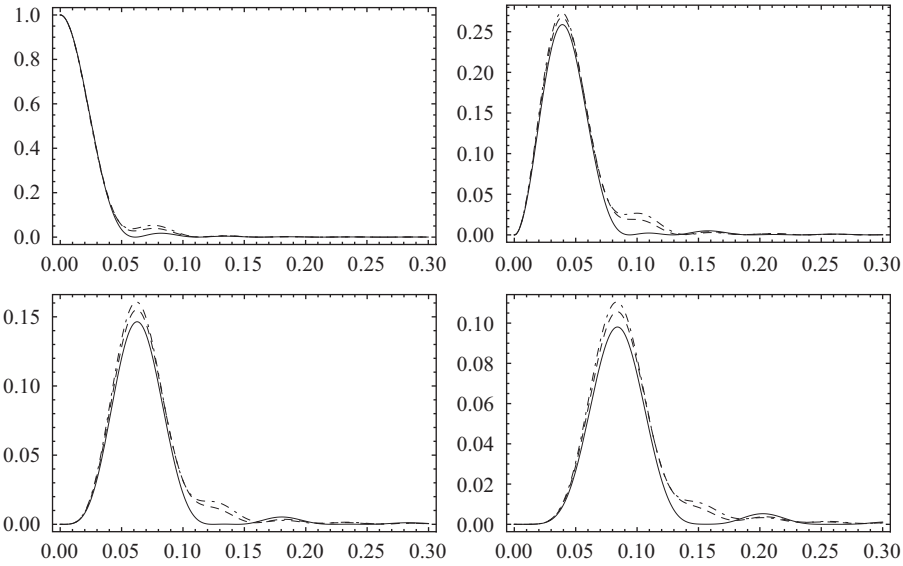

Fig. 8. Same as in Fig. 7 for a mask with 50 μm diameter. Full lines $C_s=0$ and dashed lines $C_s=1.2$ mm.

which is a function of radial distance q only, we calculate the convolution

$$I=\rho_s\otimes\rho \tag{25}$$

as

$$I(q)=\int_0^\infty \rho(\mathbf{q}')e^{-(\mathbf{q}-\mathbf{q}')^2/2\sigma^2}\,d^2q'.$$

The Gaussian can be separated into

$$e^{-(\mathbf{q}-\mathbf{q}')^2/2\sigma^2}=e^{-\mathbf{q}^2/2\sigma^2}e^{-\mathbf{q}'^2/2\sigma^2}e^{2\mathbf{q}\cdot\mathbf{q}'/2\sigma^2}.$$

Only the last factor depends on the azimuth, and the integral over the φ variable is

$$\int_0^{2\pi} e^{2qq'\cos\varphi/2\sigma^2}\,d\varphi=2\pi I_0(2qq'),$$

with the modified Bessel function of first kind and order zero, I_0. So, the convolution can be written as

$$I(q)=e^{-q^2/2\sigma^2}\int_0^\infty \rho(q')e^{-q'^2/2\sigma^2}I_0(2qq')q'\,dq'.$$

Fig. 10 shows the effect of partial coherence on the $m=1$ vortex. The central dip rises rapidly with increasing angular width of the source subtended on the aperture. This constitutes a very sensitive monitor of coherence. On the other hand, it renders the creation of pure vortices difficult. Very small sources are needed, the critical source size being inversely proportional to the mask diameter. For a 50 μm mask, the angular width of the source should not exceed 0.01 μrad in order to see a drop of the central intensity to 50%.

8. Conclusions

We have developed the theory of electrons carrying quantized orbital angular momentum. To make connection to realistic

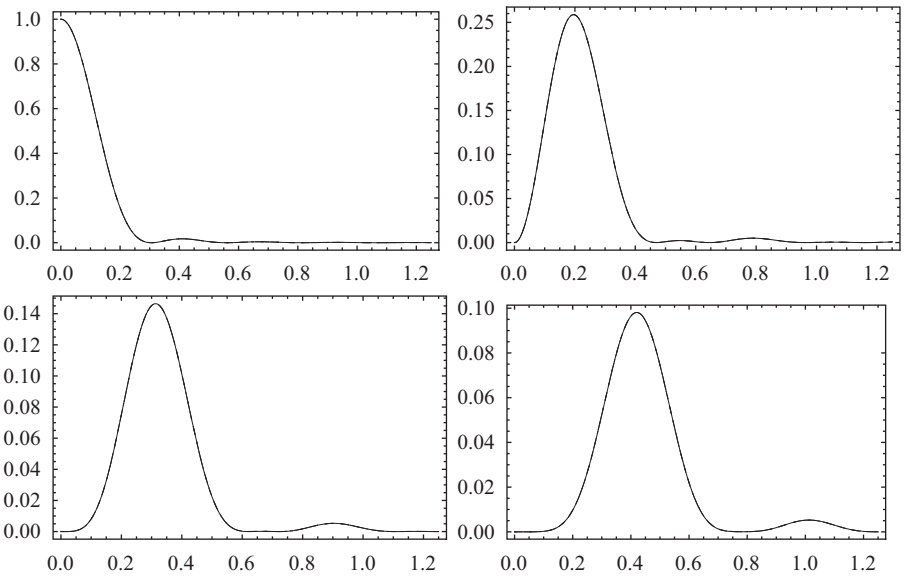

Fig. 9. Same as in Fig. 7 for a mask with 10 μm diameter. The results for the 3 C_s values coincide within the drawing accuracy.

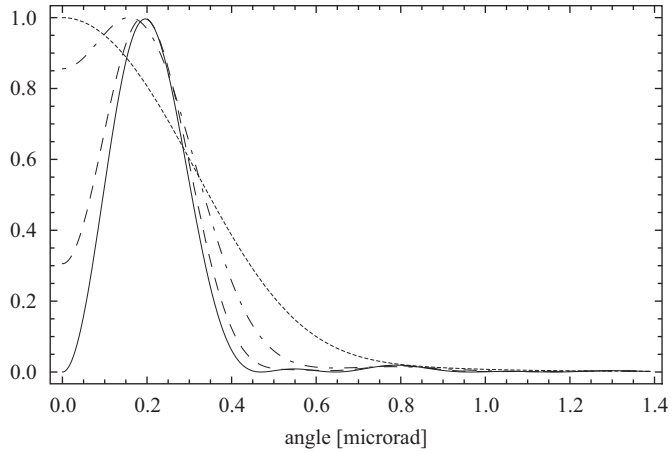

Fig. 10. Effect of a Gaussian source distribution on the $m=1$ vortex. Radial intensity profile for a mask with 10 μm diameter. All intensities scaled to 1. The abscissa is relative to the vortex center. The parameter is σ of the source subtended on the aperture: $\sigma=0$ (full line), 0.05 (dashed), 0.10 (dash-dotted), 0.15 (dotted) μrad.

situations, we considered a plane wave moving along the optic axis of a lens system, intercepted by a round, centered aperture.[8] It turns out that the movement along the optic axis can be separated off; the reduced Schrödinger equation operating in the plane of the aperture can be mapped onto Bessel's differential equation. The ensuing eigenfunctions fall into families with discrete orbital angular momentum $\hbar m$ along the optic axis where m is a magnetic quantum number. Those vortices can be produced by matching a plane wave after passage through a holographic mask with a fork dislocation to the eigenfunctions of the cylindrical problem. Vortices can be focussed by magnetic lenses into volcano-like charge distributions with very narrow angular divergence, resembling loop currents in the diffraction plane. Inclusion of spherical aberration changes the ringlike shape but does not destroy the central zero intensity of vortices with $m\neq 0$. Partial coherence of the incident wave leads to a rise of the central intensity minimum. It is shown that a very small source angle (i.e. a very high coherence) is necessary so as to keep the volcano structure intact. Their small angular width in the far field may allow the creation of nm-sized or smaller electron vortices but the demand for extremely high coherence of the source poses a serious difficulty.

[8] In the experiment, this aperture carries the holographic mask.

Acknowledgements

P.S. acknowledges the support of the Austrian Science Fund, Project I543-N20. J.V. acknowledges the financial support from the European Union under the Framework 6 Program, under a contract for an Integrated Infrastructure Initiative, Reference no. 026019 ESTEEM. We thank Karsten Held, Stefan Löffler and Inga Ennen for valuable comments.

References

[1] M. Uchida, A. Tonomura, Generation of electron beams carrying orbital angular momentum, Nature 464 (2010) 737–739.
[2] J. Verbeeck, H. Tian, P. Schattschneider, Production and application of electron vortex beams, Nature 467 (2010) 301–304.
[3] K.Y. Bliokh, Y.P. Bliokh, S. Savel'Ev, F. Nori, Semiclassical dynamics of electron wave packet states with phase vortices, Physical Review Letters 99 (2007) 190404.
[4] P. Schattschneider, S. Rubino, C. Hébert, J. Rusz, J. Kunes, P. Novák, E. Carlino, M. Fabrizioli, G. Panaccione, G. Rossi, Detection of magnetic circular dichroism using a transmission electron microscope, Nature 441 (2006) 486–488.
[5] B. McMorran, A. Agrawal, I. Anderson, A. Herzing, H. Lezec, J. McClelland, J. Unguris, Electron vortex beams with high quanta of orbital angular momentum, Science 331 (2011) 192–195.
[6] G. Molina-Terriza, J.P. Torres, L. Torner, Twisted photons, Nature Physics 3 (2007) 305–310.
[7] J. Nye, M. Berry, Dislocations in wave trains, Proceedings of the Royal Society of London, Series A 336 (1974) 165–190.
[8] J. Vaughan, D. Willetts, Temporal and interference fringe analysis of TEM_{01} laser modes, Journal of the Optical Society of America 73 (1983) 1018–1021.
[9] J. Poynting, The wave motion of a revolving shaft, and a suggestion as to the angular momentum in a beam of circularly polarized light, Proceedings of the Royal Society of London, Series A 82 (1909) 560–567.
[10] L. Allen, M. Beijersbergen, R. Spreeuw, J. Woerdman, Orbital angular momentum of light and the transformation of Laguerre–Gaussian laser modes, Physical Review A 45 (1992) 8185–8189.
[11] S.J. van Enk, G. Nienhuis, Eigenfunction description of laser beams and orbital angular momentum of light, Optics Communications 94 (1992) 147–158.
[12] W. Glaser, Grundlagen der Elektronenoptik, Springer-Verlag, Wien, 1952.
[13] P. Rez, Analytic properties of the contrast transfer function in high-resolution electron microscopy, Acta Crystallographica A 44 (1988) 946–953.

[14] P. Schattschneider, M. Nelhiebel, B. Jouffrey, The density matrix of inelastically scattered fast electrons, Physical Review B 59 (1999) 10959–10969.
[15] C. Dwyer, S.D. Findlay, L.J. Allen, Multiple elastic scattering of core-loss electrons in atomic resolution imaging, Physical Review B 77 (2008) 184107.
[16] P. Schattschneider, C. Hébert, B. Jouffrey, Orientation dependence of ionization edges in EELS, Ultramicroscopy 86 (2001) 343–353.
[17] M. Nelhiebel, N. Luchier, P. Schorsch, P. Schattschneider, B. Jouffrey, The mixed dynamic form factor for atomic core-level excitation in interferometric electron-energy-loss experiments, Philosophical Magazine B 79 (1999) 941–953.
[18] M. Nelhiebel, P.-H. Louf, P. Schattschneider, P. Blaha, K. Schwarz, B. Jouffrey, Theory of orientation-sensitive near-edge fine-structure core-level spectroscopy, Physical Review B 59 (1999) 12807–12814.